## ARTICLE IN PRESS

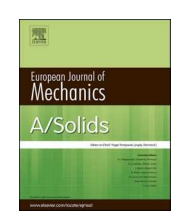
European Journal of Mechanics / A Solids xxx (xxxx) xxx

FISEVIER

Contents lists available at ScienceDirect

## European Journal of Mechanics / A Solids

journal homepage: www.elsevier.com/locate/ejmsol



## Analysis of thin layers with interphases

Kenneth M. Liechti<sup>a</sup>, Kirill R. Rebrov<sup>b</sup>, Gregory J. Rodin<sup>a,b,\*</sup>

- a Department of Aerospace Engineering and Engineering Mechanics, The University of Texas at Austin, Austin, TX, 78712, USA
- <sup>b</sup> Oden Institute for Computational Engineering and Sciences, The University of Texas at Austin, Austin, TX, 78712, USA

#### ABSTRACT

Bonds between distinct solids rarely present sharp discontinuities in mechanical properties. Particularly in the case of the bonds between polymers with metals, ceramics, and semiconductors, interphase regions are formed whose mechanical behavior differs from that of the bulk polymer. This paper examines the potential of detecting interphases associated with thin polymer layers under axial and shear loading. We demonstrate that a recent asymptotic analysis co-developed by one of our honorees can be extended and holds in the presence of interphases. As a result, we are able to establish the conditions under which interphases may be detected when thin layers are loaded in tension and shear. Further, our analysis suggests that interphases may significantly reduce the high degree of triaxiality that has long been associated with thin, nearly incompressible layers.

#### 1. Introduction

Epoxies are ubiquitous in applications ranging from primary structural adhesive joints, laminated fiber-reinforced polymers to encapsulants and molding compounds for microelectronic packaging. For many applications, the bonds formed between epoxies and their various target substrates (metals, ceramics, semiconductors, fibers, etc.) play an important role, and they should be considered as separate constitutive entities. This important point was first recognized by Sharpe (1972), who postulated that the bonds form an interphase, with properties distinct from those of the epoxy and the contact substrate. The nature of epoxy interphases has been examined by studying the migration of the amido-amine hardener to the substrate, which results in an off-stoichiometric cure near the substrate (Bouchet and Roche, 2002; Dey et al., 2014; Drzal, 1986; Roche et al., 2002; Vanlandingham et al., 1999). Interphases may also be formed when substrates are functionalized with covalent tethers to the epoxy (Drzal et al., 1983; Drzal et al., 1982; Mello and Liechti, 2006). The mechanical properties of interphases have been studied using scanning probe microscopy techniques such as Peak Force Quantitative Nano-Mechanics (PF-QNM) (Qi et al., 2019) and atomic force microscopy (Zhang et al., 2018). In the latter case, the indentation data was accompanied by an extensive finite element analysis in an attempt to account for the effect of the substrate on such data. Typically, these approaches have suggested that epoxy interphases are about 10-20 nm thick and are more compliant than the bulk epoxy. Recently Yang et al. (2021) probed interphases indirectly, by performing experiments on laminated silicon-epoxy double-cantilever beams. Using Winkler's elastic foundation model, they calculated

effective normal and shear compliances of thin epoxy layers, which turned out to be significantly higher than those one would obtain for perfectly bonded epoxy layers. Accordingly, the difference was rightfully attributed to interphases.

Interphases are also abundant in filled rubbers as well as in situations where rubbers are bonded to other substrates. In this case, the rubber molecules adhere to the stiffer substrates via combinations of van der Waals interactions, hydrogen bonding, and chemical bonding. In contrast to epoxy interphases, the rubber interphase is usually stiffer than the surrounding rubber matrix. For example, Brune et al. (2016) examined the interphase that formed in an elastomer joined to the silicon oxide surface of a silicon wafer using scanning probe microscopy coupled with finite element modeling. The interphase was 40 nm thick and was composed of a region of tightly bound rubber with thickness less than  $10\,\mathrm{nm}$  and shear modulus greater than  $250\,\mathrm{MPa}$  closer to the silicon oxide surface. This was followed by a more loosely bound rubber region with a thickness around 30 nm and shear modulus around 7 MPa. For reference, the neat polymer had a shear modulus of 0.3 MPa. A similar interphase structure has been identified by Tian et al. (2019), who examined interphase formation in a silicon-filled rubber composite using PF-QNM. The presence of the interphase was confirmed by transmission electron microscopy.

Macroscopically, it is natural to model interphases as cohesive zones (Gowrishankar et al., 2012; Liechti et al., 2000; Needleman, 1990; Sorensen and Jacobsen, 2003; Ungsuwarungsri and Knauss, 1987; Wu et al., 2019). That is, an interphase is represented by continuously distributed springs, whose deformation is characterized by relating the transmitted tractions to the displacement jumps across the interphase.

https://doi.org/10.1016/j.euromechsol.2022.104549

Received 9 December 2021; Received in revised form 1 February 2022; Accepted 2 February 2022 Available online 10 February 2022

0997-7538/© 2022 Published by Elsevier Masson SAS.

<sup>\*</sup> Corresponding author. Department of Aerospace Engineering and Engineering Mechanics, The University of Texas at Austin, Austin, TX, 78712, USA. *E-mail address*: gjr@oden.utexas.edu (G.J. Rodin).

The use of continuously distributed springs goes back to Winkler's work published in 1867; for a recent review of related models we refer to Dillard et al. (2018). Alternatively, one can model interphases in the context of Gurtin-Murdoch's surface elasticity framework (Gurtin and Murdoch, 1975, 1978; Ru, 2010), which has significantly influenced the pertinent literature. We believe that, at this stage, such an effort would be premature, as available experimental data are rather limited, and it has not been established that Winkler's model is inadequate.

If, in addition to deformation properties, the springs can be endowed with fracture properties, then cohesive zone models can be extended to nucleation and growth of cracks. This idea goes back to Barenblatt (1959) and Dugdale (1960); for a review of related models we refer to Park and Paulino (2011). Again, we believe that the use of Gurtin--Murdoch's type models (Gorbushin et al., 2020; Kim et al., 2011a, 2011b) for fracture modeling is premature due to limited experimental data. To this end, let us mention that although the mixed-mode behavior of adhesive layers and laminated composites has been extracted since the seminal work of Sorensen and Kirkegaard (2006), it is only recently that extracted traction-separation relations have been associated with interphases (Wu et al., 2019). This result has been further refined by Yang et al. (2021) using asymmetrically loaded double cantilever beam specimens, so that both normal and shear modes were independently engaged and associated spring stiffnesses were extracted. Nonetheless, there is still a concern that the strain states in the interlayer and associated interphases that are produced by the rotation of the adherends may complicate the extraction of interphase stiffnesses.

In this paper, we propose a new experimental setup for probing interphases. It involves a thin polymeric layer bonded to two very stiff plates; the term thin implies that the layer thickness is much smaller than its base dimensions. This proposal is motived by the asymptotic analysis of Movchan et al. (2021), which revealed that, under axisymmetric conditions, a thin layer of compressible material, bonded to two rigid plates, realizes *uniform* strain and stress fields almost everywhere except for small regions near the free surface. Here we demonstrate that this property holds in the presence of interphases and establish simple relationships between normal and shear stiffnesses of interphases and the overall specimen response. Consequently, the proposed experimental setup offers a very simple and unambiguous methodology for extracting the interphase stiffnesses.

The paper Movchan et al. (2021), seminal to this work, is one of the many impactful contributions of the honorees to asymptotic analysis of solids and multi-scale structures (Movchan and Movchan, 1995; Kozlov et al., 1999; Movchan et al., 2002; Maz'ya et al., 2013), wave propagation (Movchan et al., 2017), and applied mathematics education (Ockendon et al., 2003).

The proposed experimental setup goes back to Gent and Lindley (1959), who recognized that it realizes large stress concentrations conducive to cavitation in *nearly incompressible* rubbers. This point has been confirmed in multiple studies (Chalhoub and Kelly, 1990; Gent, 1994; Horton et al., 2002; Lindley, 1979; Lindsey et al., 1963; Qiao and Lu, 2015; Schapery, 2018; Tsai and Lee, 1998). In contrast, in this paper, we focus primarily on compressible layers. In the process, we demonstrate that thin layers of compressible versus nearly incompressible materials exhibit significantly different responses. Further, we show that interphases may significantly affect the response of thin nearly incompressible rubber layers.

This paper is structured as follows: In Section 2, we motivate our work and develop its foundation by examining the case of thin layers perfectly bonded to two rigid plates. In Section 3, we extend our approach to thin layers bonded to two rigid plates via interphases. In Section 4, we extend key results of Section 2 and 3 to multi-layers, followed by a discussion of some of the implications of these results in Section 5.

#### 2. Thin layers perfectly bonded to two rigid plates

In this section, we present a sequence of analytical and finite element solutions leading to a very simple approximate but nevertheless accurate analysis of thin layers bonded to two rigid plates, as long as Poisson's ratio  $\nu$  of the layer material is not too close to 1/2. We refer to such layers as thin and compressible. In contrast, if  $\nu$  is close to 1/2, we refer to layers as nearly incompressible. Of course, if  $\nu$  is equal to 1/2, we refer to such layers as incompressible.

#### 2.1. Motivational examples

Consider a homogeneous rectangular layer with a square  $L \times L$  base and thickness H perfectly bonded to two rigid plates. We describe this layer using natural Cartesian coordinates (Fig. 1):

$$-\frac{L}{2} < x < \frac{L}{2}, \quad -\frac{L}{2} < y < \frac{L}{2}, \quad -\frac{H}{2} < z < \frac{H}{2}.$$

In this subsection, our objective is to illustrate that thin compressible layers realize essentially uniform strain and stress fields in their bulk under both normal and shear loadings. The term essentially means that the strain and stress fields are very close to uniform except for a small region adjacent to the lateral faces defined by the equations  $x = \pm L/2$  or  $y = \pm L/2$ . For illustrative purposes, we consider epoxy and rubber layers perfectly bonded to rigid plates. These materials are chosen because for epoxy Poisson's ratio is  $\nu = 0.33$ , and therefore it is a good representative of compressible materials. In contrast, for rubber  $\nu =$ 0.499905 (Anderson et al., 2004), and therefore it is nearly incompressible. Fig. 2 presents four contour plots for rectangular layers subjected to shear by displacing the upper plate by  $U_x$  and the lower plate by  $-U_x$ . Each plot in Fig. 2 is for the stress  $\sigma_{xz}$  normalized by its average value as a function of x and y in the mid-plane z = 0. The contour plots for thick epoxy (Fig. 2a) and rubber (Fig. 2b) layers, characterized by H/L=1, show that the stress distributions are essentially the same and non-uniform. In contrast, for thin layers, characterized by H/L = 0.01, the contour plots for epoxy (Fig. 2c) and rubber (Fig. 2d) are essentially the same and uniform, except near the edges  $x = \pm L/2$ . Since Fig. 2 is an illustration it does not involve any numerical values.

Results shown in Fig. 2 are not surprising. First, the difference between epoxy and rubber is not essential, simply because shearing is not affected by the degree of compressibility. Second, all contour plots in Fig. 2 would be perfectly uniform if the lateral faces  $x=\pm L/2$  were subjected to appropriate shear tractions rather than kept traction-free. For the thin layers, the effect of these shear tractions is localized to small regions of size O(H) adjacent to the lateral faces  $x=\pm L/2$ . That is, the response of thin layers is in compliance with Saint-Venant's principle. For the thick layers, the effect of traction-free lateral faces  $x=\pm L/2$  affects the entire specimen, and therefore the stress distribution is

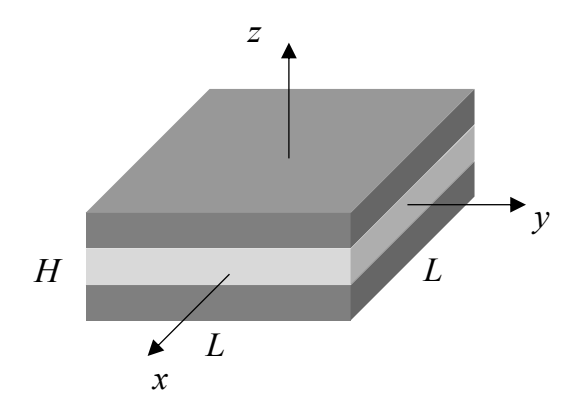
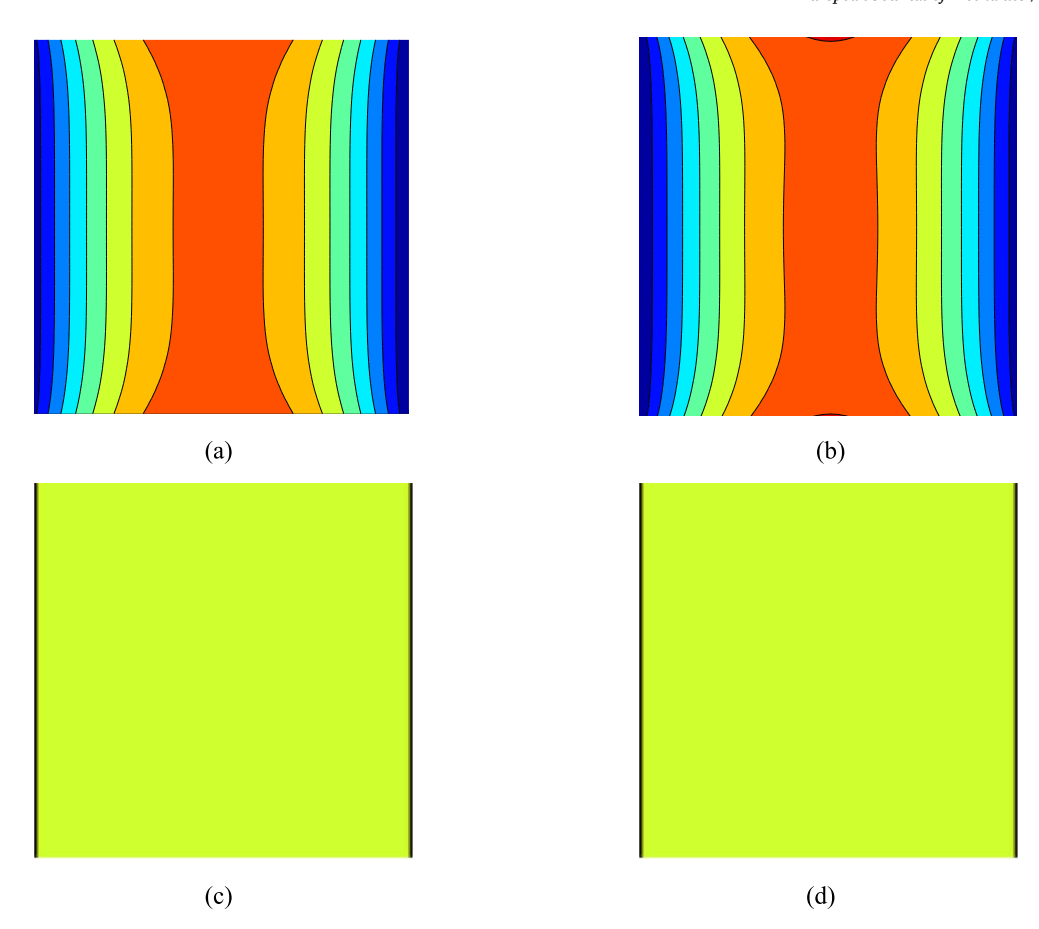


Fig. 1. A rectangular layer with a square  $L \times L$  base and thickness H constrained by two rigid plates.



**Fig. 2.** Normalized  $\sigma_{xz}$  stress distribution in the mid-plane of four layers subjected to shear: (a) epoxy layer with H/L = 1, (b) rubber layer with H/L = 1, (c) epoxy layer with H/L = 0.01, and (d) rubber layer with H/L = 0.01.

essentially non-uniform.

If the layers were subjected to boundary conditions realizing pure shear, then the elastic response of the layers would be characterized by the shear modulus. Since the lateral faces are kept traction-free, the stress and strain fields in the layers are non-uniform, and their *overall* elastic response is characterized by the *apparent* shear modulus defined as

$$\overline{G}:=rac{\langle\sigma_{xz}
angle}{\langle\gamma_{xz}
angle},$$

where the angular brackets denote volume averaging and  $\gamma$  is the engineering shear strain. For thin layers, the stress and strain fields are essentially uniform and therefore

$$\overline{G} \simeq \mu$$
. (1)

Here we use Lame's constant  $\mu$  to distinguish between the shear modulus, an intrinsic material property, and  $\overline{G}$ , an apparent property specific to thin layers. The symbol relating the left- and right-hand sides of (1) means that the sides are asymptotically equal. The contour plots shown in Fig. 3 are similar to those in Fig. 2, except that the layers were subjected to stretching by displacing the upper plate by  $U_z$  and the lower plate by  $U_z$ . Accordingly, the plots are for the normalized stress  $\sigma_{zz}$  as a function of x and y in the mid-plane z=0. It is clear that the differences between the epoxy versus rubber layers are significant, especially for the thin layers. This suggests that there are significant differences between compressible and nearly incompressible thin layers, and this issue will be addressed in Section 2.2. Here we simply observe that the stress field  $\sigma_{zz}$  is essentially uniform in the thin compressible epoxy layer, but not in the thin nearly incompressible rubber layer. Note that

contours shown in Fig. 3a,b,d look more and more circular as one moves away from the edges toward the center. This suggests that the stress field  $\sigma_{zz}$  near the center is not sensitive to the fact that the base is a square. To this end, we consider normal loading of another thin epoxy layer, which is identical to the original one, except that its base is a circle of diameter L rather than the square. The normalized  $\sigma_{zz}$  stress distributions for these two cases are compared in Fig. 4. Perhaps it is not surprising that these distributions are essentially the same. This observation allows us to examine the role of compressibility using axisymmetric deformation of circular layers.

# 2.2. Normal loading of circular cylindrical layers perfectly bonded to two rigid plates

In the previous subsection, we conjectured that thin epoxy (compressible) layers constrained by two rigid plates realize essentially uniform stress-strain states in their bulk under both shear and normal loading conditions. While this uniformity was expected under shear, its presence was somewhat surprising under normal loading conditions. Further, it appeared that the uniformity was not realized by nearly incompressible rubber layers. In this subsection, we focus on circular thin layers under axisymmetric loading conditions induced by displacing the plates by  $\pm U_z$ . Our analysis relies on the asymptotic solution of this problem developed in Movchan et al. (2021). Here we summarize key results of that work, and refer to the source for further details.

A thin circular cylindrical layer with thickness H=2h and diameter D=2a (Fig. 5) is characterized by the geometric aspect ratio

$$\xi : = \frac{H}{D} = \frac{h}{a} \tag{2}$$

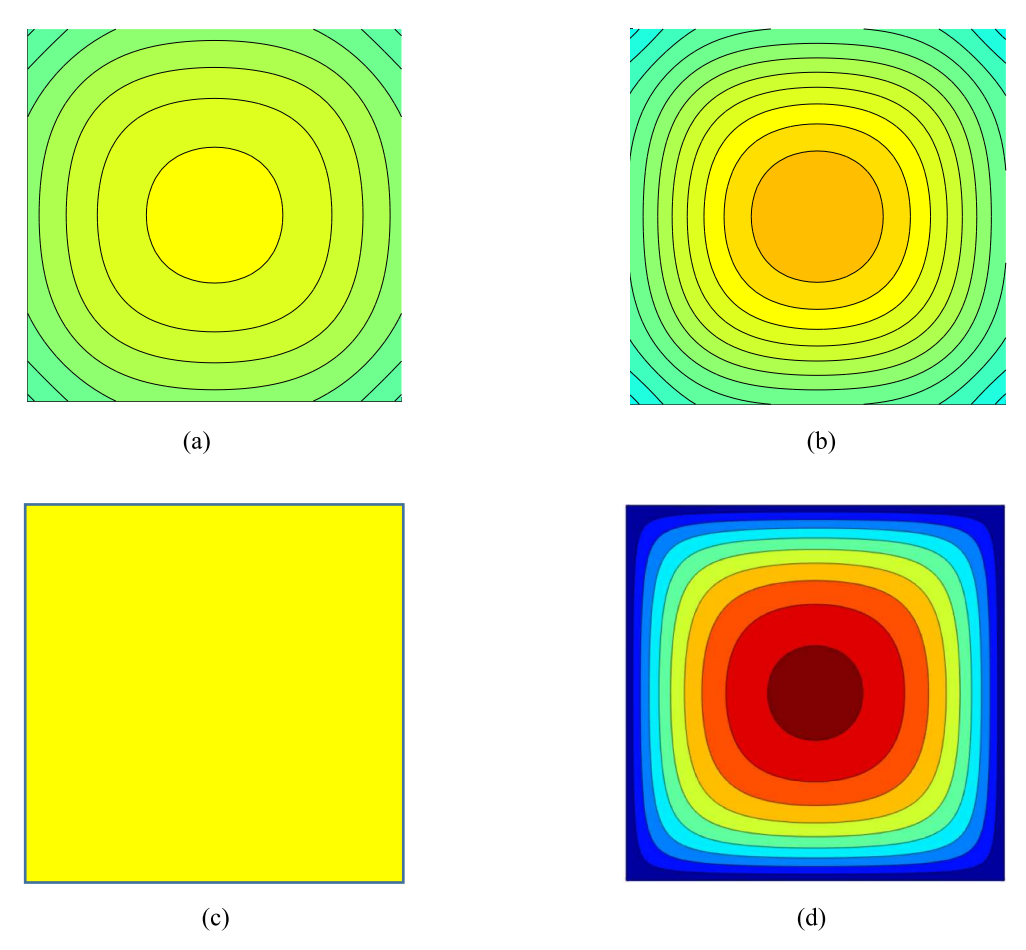


Fig. 3. Normalized  $\sigma_{zz}$  stress distribution in the mid-plane of four layers subjected to normal loading: (a) epoxy layer with H/L=1, (b) rubber layer with H/L=0.01, and (d) rubber layer with H/L=0.01.

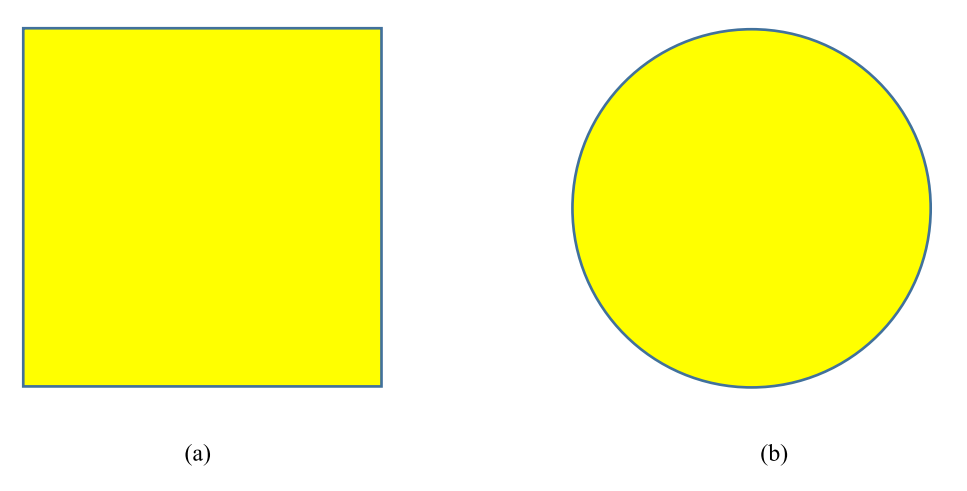


Fig. 4. Normalized  $\sigma_{zz}$  stress distributions in the mid-plane of (a) rectangular and (b) circular thin epoxy layers with H/L=0.01.

and the dimensionless material parameter (Lindsey et al., 1963)

$$\chi:=\sqrt{\frac{3(1-2\nu)}{2(1-\nu)}}.$$
 (3)

The parameter  $\chi$  arises naturally from the governing equations, and it is confined to the interval

$$\frac{3}{2} > \chi \ge 0$$
 for  $-1 < \nu \le 1/2$ . (4)

From now on we use  $\mu$  and  $\chi$  as the pair of intrinsic elastic constants, and imply that all layers under consideration are thin.

The asymptotic solution of Movchan et al. (2021) for the apparent Young's modulus is

$$\widehat{E}(\xi,\chi) := \frac{\langle \sigma_{zz} \rangle}{\langle \varepsilon_{zz} \rangle} \simeq \frac{3\mu}{\chi^2} \left\{ 1 + \frac{6(3 - 2\chi^2)\frac{\xi}{\chi} I_1\left(\frac{\chi}{\xi}\right)}{(3 - \chi^2)\left[2\xi\chi I_1\left(\frac{\chi}{\xi}\right) - 3I_0\left(\frac{\chi}{\xi}\right)\right]} \right\}.$$
 (5)

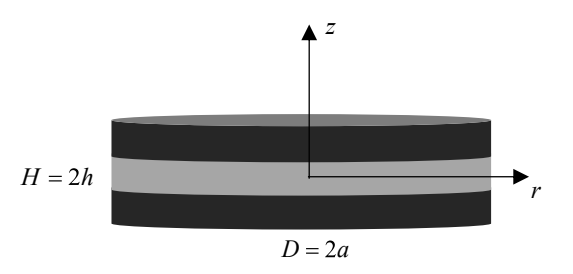


Fig. 5. A circular cylindrical layer perfectly bonded to two rigid plates.

The hat symbol denotes that this solution is valid for any  $\chi$  in the admissible interval defined in (4). In particular, for incompressible layers

$$\widetilde{E} := \lim_{\chi \to 0} \widehat{E}(\xi, \chi) \simeq \frac{3\mu}{8\xi^2}.$$
(6)

Here we use the tilde symbol to denote that this expression is restricted to incompressible materials. While this expression is commonly used in rheometry, it is of little practical use in the solid mechanics community, since the important role of compressibility has been recognized in the seminal work of Gent and Lindley (1959). For this reason, in Sections 2 through 4, we will not consider incompressible layers. Nevertheless, those layers will be discussed in Section 5, where we show that the assumption of incompressibility is further undermined in the presence of interphases.

For compressible materials, characterized by  $\chi=O(1)$ , it is meaningful to introduce the small parameter

$$\zeta := \frac{\xi}{\chi},\tag{7}$$

and rewrite (5) in the form

$$\widehat{E}(\zeta,\chi) \simeq \frac{3\mu}{\chi^2} \left\{ 1 + \frac{6(3 - 2\chi^2)\zeta I_1\left(\frac{1}{\zeta}\right)}{(3 - \chi^2)\left[2\chi^2\zeta I_1\left(\frac{1}{\zeta}\right) - 3I_0\left(\frac{1}{\zeta}\right)\right]} \right\}.$$
 (8)

Then the apparent Young's modulus for compressible material layers is

$$\overline{E} := \lim_{\zeta \to 0} \widehat{E}(\zeta, \chi) \simeq \frac{3\mu}{\gamma^2}.$$
 (9)

Here we use the bar symbol to denote that this expression is restricted to compressible layers.

Note that (6) and (8) imply that  $\tilde{E}$  is not a material property, whereas  $\overline{E}$  can be treated as one. The second half of this statement is a consequence of the essential uniformity of the strain and stress fields in compressible material layers. Those fields are very simple, and their non-zero components are

$$arepsilon_{zz} \simeq rac{U_z}{h}$$

and

$$\sigma_{rr} = \sigma_{\theta\theta} \simeq \frac{(3-2\chi^2)\mu}{\chi^2} \frac{U_z}{h}$$

$$\sigma_{zz} \simeq \frac{3\mu}{\gamma^2} \frac{U_z}{h}.$$

These fields also characterize laterally constrained uniaxial stretching of the layer. Thus, in a compressible layer, the constraints imposed by perfectly bonded plates are equivalent to those imposed by perfectly lubricated plates and a cylindrical confinement.

Note that while  $\zeta$  was introduced as a small parameter for characterizing thin compressible layers, formally,  $\zeta$  can be extended to nearly

incompressible layers, and even incompressible layers, for which  $\zeta \to \infty$ . Thus  $\zeta$  can be adopted as a measure of compressibility of thin constrained layers. Further, it is meaningful to associate nearly incompressible layers with  $\zeta = O(1)$ . For example, a layer with  $\xi = 0.01$  and  $\nu = 0.49$  results in  $\zeta = 0.04$ «1, and therefore the layer is characterized as compressible! But, for the thin rubber layer considered in Section 2.1, with  $\xi = 0.01$  and  $\nu = 0.499905$ ,  $\zeta \approx 0.4 = O(1)$ , and therefore it is characterized as nearly incompressible.

#### 2.3. Verification of the approximate solution for single layers

In this subsection, we are concerned with evaluating the approximations in (1) and (9) for the apparent moduli  $\overline{E}$  and  $\overline{G}$  for homogeneous rectangular compressible layers perfectly bonded to two rigid plates (Fig. 1). To this end,  $\overline{E}$  and  $\overline{G}$  are compared with the corresponding moduli obtained from convergent finite element solutions, denoted by  $E_{FE}$  and  $G_{FE}$ , which are treated as the benchmarks. All results reported herein are for epoxy layers for which

$$\mu = 1.13 \text{ GPa}$$
 and  $\chi = 0.872$ .

These material properties result in the apparent properties

$$\overline{E} = 4.44 \text{ GPa}$$
 and  $\overline{G} = 1.13 \text{ GPa}$ .

We evaluated these predictions for three epoxy layers and compiled results in Table 1. It is clear that the accuracy of both  $\overline{E}$  and  $\overline{G}$  improves by an order of magnitude as  $\xi$  decreases by an order of magnitude. Further, the accuracy is better than one percent for layers with  $\xi \leq 10^{-2}$ . Results compiled in Table 1 for fully three-dimensional problems are consistent with more detailed evaluations for  $\overline{E}$  based on axisymmetric problems for circular layers in Movchan et al. (2021). In particular, the data there supports the trend

$$\frac{|\overline{E} - E_{\mathit{FE}}|}{E_{\mathit{FE}}} = O(\xi) \quad \text{and} \quad \frac{|\overline{G} - G_{\mathit{FE}}|}{G_{\mathit{FE}}} = O(\xi).$$

#### 3. Thin layers bonded to two rigid plates via interphases

#### 3.1. Interphases

In this section, we consider layers bonded to rigid plates via interphases, modeled as distributed springs with the normal stiffness  $k_N$  and shear stiffness  $k_S$ . As far as analysis is concerned, an interphase between two layers modifies the displacement continuity conditions so that the jumps in the normal and tangential displacements are proportional to the corresponding traction components:

$$[\![u_N]\!] = \frac{t_N}{k_N} \text{ and } [\![u_S]\!] = \frac{t_S}{k_N}.$$
 (10)

Here the brackets denote the jump across the interphase. Of course, the continuity condition on the tractions

$$t_N = t_S = 0$$

is unaffected by the interphase as it is solely dictated by equilibrium. For an interphase between a layer and a rigid plate, (10) implies:

$$t_N = k_N(U_N - u_N)$$
 and  $t_S = k_S(U_S - u_S)$ , (11)

Table 1

Apparent moduli  $\overline{E}$  and  $\overline{G}$  for epoxy rectangular layers versus the corresponding predictions obtained from convergent finite element solutions.

	$\xi=10^{-3}$	$\xi=10^{-2}$	$\xi=10^{-1}$
$ \overline{E}-E_{FE} /E_{FE}$	$4  imes 10^{-4}$	$6  imes 10^{-3}$	$6  imes 10^{-2}$
$ \overline{G}-G_{FE} /G_{FE}$	$1  imes 10^{-4}$	$3  imes 10^{-3}$	$3 imes10^{-2}$

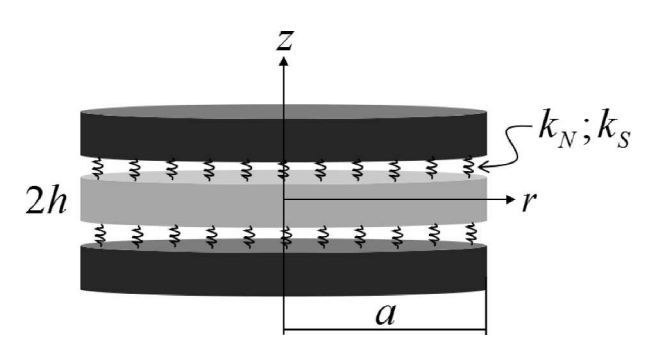


Fig. 6. A circular cylindrical layer bonded to two rigid plates via interphases.

where  $U_N$  and  $U_S$  are the plate displacements.

#### 3.2. Axisymmetric loading of a circular cylindrical layer

Consider a circular layer bonded to two rigid plates via identical interphases with the stiffnesses  $k_N$  and  $k_S$  (Fig. 6). Under axisymmetric loading, the boundary conditions on the flat surfaces follow from (11)

$$z = \pm h$$
,  $k_N(u_z \mp U_z) + \sigma_{zz} = 0$ ,  $k_S u_r + \sigma_{rz} = 0$ . (12)

On the cylindrical traction-free surface, the boundary conditions are

$$r = a$$
,  $\sigma_{rr} = 0$  and  $\sigma_{rz} = 0$ .

In the asymptotic setting, these boundary conditions are to be satisfied in Saint-Venant's sense:

$$r=a$$
, 
$$\int_{-h}^{h} \sigma_{rr} dz = \int_{-h}^{h} \sigma_{rz} dz = 0.$$
 (13)

We solve the arising boundary-value problem of classical elasticity following Movchan et al. (2021). Accordingly, the displacements are represented in terms of a Love-Galerkin's potential  $\Phi$ , so that

$$u_r = -\frac{1}{2(1-\nu)} \frac{\partial^2 \Phi}{\partial r \partial z},$$

$$u_z = \frac{\partial^2 \Phi}{\partial r^2} + \frac{1}{r} \frac{\partial \Phi}{\partial r} + \frac{1-2\nu}{2(1-\nu)} \frac{\partial^2 \Phi}{\partial z^2}.$$
(14)

The potential must satisfy the bi-harmonic equation

$$\left(\frac{\partial^2}{\partial r^2} + \frac{1}{r}\frac{\partial}{\partial r} + \frac{\partial^2}{\partial z^2}\right)^2 \Phi = 0.$$
 (15)

Next, to exploit the smallness of  $\xi$ , we define the scaled coordinates

$$R:=\frac{r}{a}$$
 and  $Z:=\frac{z}{h}=\frac{z}{a\xi}$ .

and therefore the potential is expressed in the form

$$\Phi \simeq A_3(R)Z^3 + A_2(R)Z^2 + A_1(R)Z + A_0(R) . \tag{16}$$

Up to a constant C, the functions of R in this equation are determined by enforcing the boundary conditions in (12):

$$A_0(R) = A_2(R) \simeq 0,$$

$$A_1(R) \simeq \frac{3[12 - (3 - \chi^2)(8 + \beta_S)]}{(3 - \chi^2)\beta_S} A_3(R), \tag{17}$$

$$A_3(R)\simeq rac{a^2\xi^2U_zeta_N}{2\chi^2(2+eta_N)}+CI_0igg(rac{R}{\zeta^*}igg).$$

Here

$$\beta_N := \frac{k_N H}{\overline{E}} = \frac{2k_N h}{\overline{E}} \quad \text{and} \quad \beta_S := \frac{k_S H}{\mu} = \frac{2k_S h}{\mu}$$
 (18)

are normalized stiffnesses of the distributed springs,  $I_0$  is a Bessel function, and

$$\zeta^* := \zeta \sqrt{\frac{[6(3-2\chi^2)+(3-\chi^2)\beta_S]\beta_N}{(3-\chi^2)(2+\beta_N)\beta_S}}.$$
 (19)

The parameter  $\zeta^*$  is a generalization of  $\zeta$  defined in (7), and we use the asterisk to denote that this definition involves the interphases. In particular

$$\zeta = \lim_{\beta_N \to \infty} \zeta^*.$$

$$\beta_s \to \infty$$

The constant C in (17) is obtained by imposing the boundary conditions in (13). The first of these conditions yields

$$C \simeq \frac{3a^{2}\xi^{2}U_{z}(3-2\chi^{2})\beta_{N}^{2}}{2\chi^{2}(2+\beta_{N})\left\{2\chi^{2}(3-\chi^{2})(2+\beta_{N})\zeta^{*}I_{1}\left(\frac{1}{\zeta^{*}}\right)-3[2\chi^{2}+(3-\chi^{2})\beta_{N}]I_{0}\left(\frac{1}{\zeta^{*}}\right)\right\}},$$
(20)

whereas the second condition is trivially satisfied due to symmetry about the plane z=0.

The potential  $\Phi$  allows us to calculate the displacement, strain, and stress fields. Their expressions are lengthy and therefore not stated. For our purposes, it is important to calculate the force transmitted through the system,

$$F = \int_{-\infty}^{a} \sigma_{zz|z=h} 2\pi r dr = 2\pi a^{2} \int_{-\infty}^{1} \sigma_{zz|Z=1} R dR,$$

which leads directly to

$$\widehat{E}^*(\zeta^*, \chi) \simeq \frac{3\mu\beta_N}{\chi^2(2+\beta_N)} \left\{ 1 + \frac{6(3-2\chi^2)\beta_N\zeta^*I_1\left(\frac{1}{\zeta^*}\right)}{2\chi^2(3-\chi^2)(2+\beta_N)\zeta^*I_1\left(\frac{1}{\zeta^*}\right) - 3[2\chi^2 + (3-\chi^2)\beta_N]I_0\left(\frac{1}{\zeta^*}\right)} \right\}. \tag{21}$$

Then the asymptotic approximation for the bi-harmonic operator in (15) takes the form

$$\left(\frac{\partial^2}{\partial r^2} + \frac{1}{r}\frac{\partial}{\partial r} + \frac{\partial^2}{\partial z^2}\right)^2 = \frac{1}{a^4} \left(\frac{\partial^2}{\partial R^2} + \frac{1}{R}\frac{\partial}{\partial R} + \frac{1}{\xi^2}\frac{\partial^2}{\partial Z^2}\right)^2 \simeq \frac{1}{a^4 \xi^4} \frac{\partial^4}{\partial Z^4},$$

Here we calculated the force acting on the upper plate z=h but any z- plane would be acceptable for the calculation. Of course,  $\widehat{E}^*$  is a generalization of  $\widehat{E}$  defined in (8), and they are naturally related

$$\widehat{E}(\zeta,\chi) = \lim_{\beta_N \to \infty} \widehat{E}^*(\zeta^*,\chi)$$

$$\beta_c \to \infty$$

Similar to (9), (21) yields the expression

$$\overline{E}^* = \lim_{\zeta^* \to 0} \widehat{E}^* [\zeta^*, \chi] \simeq \frac{3\mu \beta_N}{\chi^2 (2 + \beta_N)} = \overline{E} \frac{\beta_N}{2 + \beta_N}. \tag{22}$$

This expression is somewhat surprising as it yields  $\overline{E}^*$  independent of  $\beta_S$ . This point will be examined in Sections 3.3 and 3.4.

#### 3.3. Validity of the asymptotic solutions

In this subsection, we compare the asymptotic solutions for  $\widehat{E}^*$  and  $\overline{E}^*$ , given in (21) and (22), respectively, with convergent finite element solutions. This choice differs from that made in Section 2.3 where we focused on  $\overline{E}$  rather than  $\widehat{E}$ , as there we were confident in  $\widehat{E}$  based on verification studies in Movchan et al. (2021), and the objective there was to evaluate  $\overline{E}$  and  $\overline{G}$  for thin compressible layers. In this subsection, we consider  $\widehat{E}^*$  and  $\overline{E}^*$ , with the provision that they cannot be accurate for sufficiently small  $\beta_S$ , because the case of  $\beta_S=0$  corresponds to laterally unconstrained uniaxial stretching, while the asymptotic solution implies that compressible layers are fully constrained in the lateral direction.

Since the parametric space for  $\widehat{E}^*/\mu$  and  $\overline{E}^*/\mu$  is four-dimensional, and we have already established that the asymptotic solution is accurate for  $\xi \ll 1$ , any value of  $\chi$ , and  $\beta_N, \beta_S \to \infty$ , here we focus on the parameters  $\beta_N$  and  $\beta_S$ . To this end, we set  $\xi = 10^{-2}$  and explore the parametric space spanned by  $\beta_N$  and  $\beta_S$  for epoxy and rubber layers. Comparisons are presented in Table 2 (epoxy) and 3 (rubber).

Each colored cell of Tables 2 and 3 contains two numbers; the upper number is the error for  $\widehat{E}^*$  and the lower number is the error for  $\overline{E}^*$ . The colors are assigned as follows: (i) if the error for both  $\widehat{E}^*$  and  $\overline{E}^*$  exceeds 1%, then the cell is colored red; (ii) if the error for  $\overline{E}^*$  but not  $\widehat{E}^*$  exceeds 1%, then the cell is colored yellow; and (iii) if the error for both  $\widehat{E}^*$  and  $\overline{E}^*$  is less than 1%, then the cell is colored green.

It is clear that both  $\widehat{E}^*$  and  $\overline{E}^*$  are not accurate for both epoxy and

rubber layers for sufficiently small  $\beta_S$ . But this is where similarities end, as for the epoxy layer  $\overline{E}^*$  is essentially as accurate as  $\widehat{E}^*$ , whereas for the rubber layer  $\overline{E}^*$  is inaccurate in the entire parametric domain. This statement is consistent with the fact that Table 2 contains no yellow cells, and Table 3 contains no green cells. Further, for the epoxy layer, both  $\widehat{E}^*$  and  $\overline{E}^*$  are accurate if both  $\beta_N$  and  $\beta_S$  are small. In contrast, for the rubber layer,  $\beta_N$  has essentially no bearing on the accuracy of  $\widehat{E}^*$  and  $\overline{E}^*$ .

#### 3.4. Properly constrained layers

In this subsection, we focus on explaining the results presented in Tables 2 and 3 We refer to layers for which at least  $\widehat{E}^*$  is accurate as properly constrained. Those layers are represented by yellow and green cells, and characterized by sufficiently large  $\beta_S$ .

First, let us consider improperly constrained compressible layers, characterized by  $\chi=O(1),$   $\beta_S\ll 1$ , and  $\beta_N\gg 1$ . To this end we observe that  $\widehat{E}^*$  depends on  $\beta_S$  only because  $\zeta^*$  depends on  $\beta_S$ , and therefore, it is sufficient to focus on  $\zeta^*$ . For  $\chi=O(1),$   $\beta_S\ll 1$ , and  $\beta_N\gg 1$ , (19) is well approximated by

$$\zeta^* \approx \zeta \sqrt{\frac{6(3-2\chi^2)}{3-\chi^2}} \sqrt{\frac{1}{\beta_S}},$$

which implies that large  $\zeta^*\gg 1$  is possible even for compressible layers with  $\zeta\ll 1$ . That is, a compressible layer perfectly bonded to rigid plates is characterized by  $\zeta^*=\zeta\ll 1$ . However, if the same layer is improperly constrained, it is characterized by  $\zeta^*\gg 1$ , and Bessel's functions in (21) behave rather differently for small verses large  $\zeta^*$ .

For  $\chi = O(1)$ ,  $\beta_S \ll 1$ , and  $\beta_N \ll 1$ , (19) yields the approximation

$$\zeta^* pprox \zeta \sqrt{rac{3(3-2\chi^2)}{3-\chi^2}} \sqrt{rac{eta_N}{eta_S}},$$

which explains why small  $\beta_N$  can mediate the effect of small  $\beta_S$ . For nearly incompressible layers, characterized by  $\chi \ll 1$  and  $\zeta =$ 

The relative error for the asymptotic solutions versus convergent finite solutions for the apparent moduli  $\widehat{E}^*$ ,  $\overline{E}^*$  for an epoxy layer with  $\xi=10^{-2}$ . Color red is assigned to cases in which the errors for both  $\widehat{E}^*$  and  $\overline{E}^*$  are above 1%. Color green is assigned to cases in which the errors for both  $\widehat{E}^*$  and  $\overline{E}^*$  are below 1%.

$\begin{array}{ c c } &  \hat{E}^* - E_{\mathit{FE}}  / E_{\mathit{FE}} \\ &  \bar{E}^* - E_{\mathit{FE}}  / E_{\mathit{FE}} \end{array}$	$\beta_S = 1/100$	$\beta_S = 1/10$	$\beta_S = 1$	$\beta_S = 10$	$\beta_{S} = 100$
$\beta_N = 100$	$2 \times 10^{-1}$ $1 \times 10^{-1}$	$5 \times 10^{-2}$ $4 \times 10^{-2}$	$   \begin{array}{c}     2 \times 10^{-2} \\     1 \times 10^{-2}   \end{array} $	$   \begin{array}{c}     1 \times 10^{-2} \\     7 \times 10^{-3}   \end{array} $	$9 \times 10^{-3}$ $6 \times 10^{-3}$
$\beta_N = 10$	$2 \times 10^{-1}$ $1 \times 10^{-1}$	$5 \times 10^{-2}$ $4 \times 10^{-2}$	$   \begin{array}{c}     2 \times 10^{-2} \\     1 \times 10^{-2}   \end{array} $	$9 \times 10^{-3}$ $6 \times 10^{-3}$	$8 \times 10^{-3}$ $5 \times 10^{-3}$
$\beta_N = 1$	$6 \times 10^{-2}$ $5 \times 10^{-2}$	$   \begin{array}{c}     2 \times 10^{-2} \\     2 \times 10^{-2}   \end{array} $	$6 \times 10^{-3}$ $5 \times 10^{-3}$	$3 \times 10^{-3}$ $3 \times 10^{-3}$	$3 \times 10^{-3}$ $2 \times 10^{-3}$
$\beta_N = 1/10$	$1 \times 10^{-3}$ $8 \times 10^{-3}$	$4 \times 10^{-4}$ $2 \times 10^{-3}$	1×10 <sup>-4</sup> 8×10 <sup>-4</sup>	$1 \times 10^{-4}$ $4 \times 10^{-4}$	$9 \times 10^{-5}$ $3 \times 10^{-4}$
$\beta_N = 1/100$	5×10 <sup>-4</sup> 8×10 <sup>-4</sup>	2×10 <sup>-4</sup> 3×10 <sup>-4</sup>	$5 \times 10^{-5}$ $9 \times 10^{-5}$	$4 \times 10^{-5}$ $4 \times 10^{-5}$	$4 \times 10^{-5}$ $4 \times 10^{-5}$

Table 3

The relative error for the asymptotic solutions versus convergent finite solutions for the apparent moduli  $\widehat{E}^*$ ,  $\overline{E}^*$  for a rubber layer with  $\xi=10^{-2}$ . Color red is assigned to cases in which the error for  $\widehat{E}^*$  and  $\overline{E}^*$  exceed 1%. Color yellow is assigned to cases in which the error for  $\widehat{E}^*$  is below 1% but the error for  $\overline{E}^*$  is above 1%.

$\begin{array}{ c c } \hline  \hat{E}^* - E_{FE}  / E_{FE} \\ \hline  \bar{E}^* - E_{FE}  / E_{FE} \\ \hline \end{array}$	$\beta_S = 1/100$	$\beta_S = 1/10$	$\beta_S = 1$	$\beta_S = 10$	$\beta_{\rm S}=100$
$\beta_N = 100$	$3\times10^{-1}$ $6\times10^{2}$	$5 \times 10^{-2}$ $8 \times 10^{1}$	$5 \times 10^{-3}$ $1 \times 10^{1}$	$7 \times 10^{-4}$ $3 \times 10^{0}$	$2 \times 10^{-3}$ $2 \times 10^{0}$
$\beta_N = 10$	$3\times10^{-1}$ $5\times10^{2}$	$5 \times 10^{-2}$ $7 \times 10^{1}$	$5 \times 10^{-3}$ $8 \times 10^{0}$	$7 \times 10^{-4}$ $2 \times 10^{0}$	$2 \times 10^{-3}$ $2 \times 10^{0}$
$\beta_N = 1$	$3 \times 10^{-1}$ $2 \times 10^{2}$	$5 \times 10^{-2}$ $3 \times 10^{1}$	$4 \times 10^{-3}$ $4 \times 10^{0}$	$5 \times 10^{-4}$ $1 \times 10^{0}$	$1 \times 10^{-3}$ $8 \times 10^{-1}$
$\beta_N = 1/10$	$3 \times 10^{-1}$ $3 \times 10^{1}$	$4 \times 10^{-2}$ $4 \times 10^{0}$	$4 \times 10^{-3}$ $7 \times 10^{-1}$	$5 \times 10^{-4}$ $3 \times 10^{-1}$	$2 \times 10^{-4}$ $2 \times 10^{-1}$
$\beta_N = 1/100$	$3 \times 10^{-1}$ $3 \times 10^{0}$	$3 \times 10^{-2}$ $6 \times 10^{-1}$	$7 \times 10^{-3} \\ 2 \times 10^{-1}$	$   \begin{array}{c}     3 \times 10^{-3} \\     7 \times 10^{-2}   \end{array} $	$   \begin{array}{c}     2 \times 10^{-3} \\     6 \times 10^{-2}   \end{array} $

O(1), (19) is approximated as

$$\zeta^* pprox \zeta \sqrt{rac{6}{eta_S}} \sqrt{rac{eta_N}{(2+eta_N)}}.$$

This expression explains why  $\beta_S \ll 1$  results in improperly constrained nearly incompressible layers, but it does not explain why in Table 3  $\beta_N$  has essentially has no bearing on the accuracy of  $\widehat{E}^*$  and  $\overline{E}^*$ . To this end, let us revisit the definitions for  $\beta_N$  and  $\beta_S$  in (18), which were conceived with compressible layers in mind. Accordingly  $\beta_N$  is defined by normalizing  $k_N$  with  $\overline{E}$ , and  $\beta_S$  is defined by normalizing  $k_S$  with  $\mu$ . For nearly incompressible layers, (9) implies  $\overline{E} \gg \mu$ , so that even if both  $\beta_N$  and  $\beta_S$  are small, it is still possible to have  $k_S \ll k_N$ . To address this inconsistency, one has to replace (18) with normalizations appropriate for nearly incompressible layers. We will not pursue this delicate issue in this work.

#### 4. Properly constrained compressible multilayers

In this section, we extend key results from Sections 2 and 3 to compressible multilayers with and without interphases.

#### 4.1. Single layer

Comparisons of asymptotic and finite element solutions presented in Table 2 suggest that  $\overline{E}^*$  defined in (22) is an accurate approximation for the apparent Young's modulus for properly constrained compressible layers. Equation (22) is straightforward to adopt for calculating the normal stiffness of the distributed springs, provided that  $\overline{E}^*$  has been determined experimentally:

$$\beta_N = \frac{2\overline{E}^*}{\overline{E} - \overline{E}^*}.\tag{23}$$

Together with (18) this equation yields the equation for calculating the normal stiffness in terms of the apparent moduli:

$$k_N = \frac{2}{H} \left( \frac{1}{\overline{E}^*} - \frac{1}{\overline{E}} \right)^{-1}$$
 (24)

This equation can be rewritten as

$$\frac{H}{\overline{E}^*} = \frac{H}{\overline{E}} + 2\left(\frac{1}{k_N}\right). \tag{25}$$

This form leads to a very useful interpretation: the overall system compliance  $H/\overline{E}$  is the compliance of the layer  $H/\overline{E}$  plus the compliance of the two interphases. Thus, the layer and two interphases can be thought as three layers of distributed springs connected in series, and the stiffness of the distributed springs representing the layer is  $\overline{E}/H$ . Equation (25) can be adopted for calculating the apparent shear modulus:

$$\frac{H}{\overline{G}} = \frac{H}{\overline{G}} + 2\left(\frac{1}{k_S}\right) = \frac{H}{\mu} + \frac{2}{k_S} \tag{26}$$

and

$$k_{S} = \frac{2}{H} \left( \frac{1}{C} - \frac{1}{u} \right)^{-1}. \tag{27}$$

Thus equations (24) and (27) provide a simple and unambiguous way of determining the stiffnesses  $k_N$  and  $k_S$  in terms of the intrinsic material properties of the layer,  $\overline{E}$  and  $\mu$ , its thickness H, and the apparent moduli  $\overline{E}^*$  and  $\overline{G}^*$ .

#### 4.2. Compressible multi-layers perfectly bonded to two rigid plates

The simplicity of solutions for a single compressible layer perfectly bonded to two rigid plates can be extended to multilayers. Consider a multilayer formed by N monolayers perfectly bonded to each other, and to two constraining rigid plates. Each monolayer is characterized by its apparent Young's modulus  $\overline{E}$ , shear modulus G, and thickness H.

Normal loading of the multilayer can be easily analyzed by regarding it as a system of N linearly elastic elements connected in series. Those elements transmit the same force (or average normal stress  $\langle \sigma_{zz} \rangle$ ) and their elongations are proportional to their compliances. Accordingly, the

governing equations are

Equilibrium : 
$$\langle \sigma_{zz}^{(i)} \rangle = \langle \sigma_{zz} \rangle$$

Hooke's law: 
$$\Delta u_z^{(i)} = \frac{\left\langle \sigma_{zz}^{(i)} \right\rangle H^{(i)}}{\overline{E}^{(i)}}$$
 (28)

Compatibility : 
$$\sum_{i=1}^{N} \Delta u_z^{(i)} = \Delta U_z$$
.

Here  $\langle \sigma_{zz}^{(i)} \rangle$  is the average stress in the *i*th layer,  $\Delta u_z^{(i)}$  is the axial elongation in the ith layer, and  $\Delta U_z$  is the total axial elongation of the multilayer. The governing equations are straightforward to combine to calculate the apparent Young's modulus of the multi-layer:

$$\overline{E} = \frac{\sum_{i=1}^{N} H^{(i)}}{\sum_{i=1}^{N} \overline{E^{(i)}}}.$$
(29)

If a rectangular multi-layer is subjected to shear in the y-z plane, the governing equations are essentially the same

Equilibrium :  $\left\langle \tau_{yz}^{(i)} \right\rangle = \left\langle \tau_{yz} \right\rangle$ 

Hooke's law:  $\Delta u_y^{(i)} = \frac{\tau^{(i)} H^{(i)}}{\overline{C}^{(i)}}$ 

Compatibility:  $\sum_{i=1}^{N} \Delta u_y^{(i)} = \Delta U_y$ .

The notation here is self-explanatory. Similar to (29) the apparent shear modulus of the multi-layer is given by the equation

$$\overline{G} = \frac{\sum_{i=1}^{N} H^{(i)}}{\sum_{j=1}^{N} G^{(i)}}.$$
(30)

#### 4.3. Verification of the approximate solution for tri-layers with highcontrast properties

In this subsection, we consider circular tri-layers in which the interior compressible layer is sandwiched between two identical compressible exterior layers (Fig. 7). We denote the properties of the interior layer by  $\overline{E}^{(i)}$  and  $H^{(i)}$ , and the properties of the exterior layers by  $\overline{E}^{(e)}$  and  $H^{(e)}$ , so that (29) implies

$$\overline{E} = \frac{H^{(i)} + 2H^{(e)}}{\frac{H^{(i)}}{\overline{E}^{(i)}} + 2\frac{H^{(e)}}{\overline{E}^{(e)}}}.$$
(31)

We evaluated this approximation by setting  $\nu^{(i)} = \nu^{(e)} = 0.33$  and

$$\xi = \frac{H^{(i)} + 2H^{(e)}}{D} = \frac{1}{100}$$



Fig. 7. A tri-layer formed by an interior layer and two identical exterior layers perfectly bonded to two rigid plates. The properties of the interior layer are  $\overline{E}^{(i)}$  $H^{(i)}$ , and the properties of the exterior layers are  $\overline{E}^{(e)}, H^{(e)}$ .

#### Table 4

Approximation error  $|\overline{E} - E_{FE}|/E_{FE}$  for thin circular tri-layers with extreme

$ \overline{E} - E_{FE} /E_{FE}$	$2H^{(e)}/H^{(i)} = 1/100$	$2H^{(e)}/H^{(i)} = 100$
$\overline{\it E}^{(e)}/\overline{\it E}^{(i)}=1/100$	$6  imes 10^{-3}$	$5\times 10^{-3}$
$\overline{E}^{(e)}/\overline{E}^{(i)} = 100$	$6  imes 10^{-3}$	$3 imes10^{-3}$

For these fixed parameters, we considered two high-contrast ratios

$$\frac{\overline{E}^{(e)}}{\overline{F}^{(i)}} = 1 \times 10^{-2} \text{ or } 100 \text{ and } \frac{2H^{(e)}}{H^{(i)}} = 1 \times 10^{-2} \text{ or } 100.$$

Thus  $\overline{E}$  was evaluated for four extreme cases. The results for the approximation errors for  $\overline{E}$  are compiled in Table 4. It is clear that the accuracy of (23) is essentially independent of the values of  $\overline{E}^{(e)}/\overline{E}^{(i)}$  and  $H^{(e)}/H^{(i)}$ . Furthermore, the errors in Table 4 are comparable to those compiled in Table 1 for  $\xi = 1/100$ . Based on these results, we conjecture that the approximation errors for compressible, constrained multi-layers are small and essentially independent of their compositional details, so that (31) holds in general.

#### 4.4. Properly constrained compressible multi-layer with interphases

In this subsection, we combine the analyses of properly constrained monolayers with interphases in 4.1 and of perfectly bonded multilayers presented in Section 4.2 to analyze properly-constrained multilayers with interphases. Thus, per Section 3.4, we assume that each layer is compressible ( $\zeta \ll 1$ ) and for each interphase the ratio  $\beta_S/\beta_N$  is sufficiently large. Further, per Section 4.1, we treat both monolayers and interphases as elastic elements connected in series. Then, for N layers and N+1 interphases, (29) and (30) are generalized as

$$\overline{E}^* = \frac{\sum_{i=1}^{N} H^{(i)}}{\sum_{i=1}^{N} \frac{H^{(i)}}{\overline{E}^{(i)}} + \sum_{i=1}^{N+1} \frac{1}{k_{ij}^{(i)}}}$$

and

$$\overline{G}^* = \frac{\sum\limits_{i=1}^{N} H^{(i)}}{\sum\limits_{i=1}^{N} \frac{H^{(i)}}{\overline{G}^{(i)}} + \sum\limits_{i=1}^{N+1} \frac{1}{k_s^{(i)}}},$$

respectively. Of course, similar to (23) through (26) these equations can be adopted for determining  $k_N^{(i)}$  and  $k_S^{(i)}$  from measurements of  $\overline{E}^*$  and  $\overline{G}^*$ .

#### 5. Discussion

With a view of determining interphase stiffness values from normal and shear loadings of thin polymer layers, we now examine the sensitivity of load-displacement responses to the presence of interphases. The natural vehicles for addressing this issue are the apparent moduli  $\hat{E}$ (Eqn. (8)) and  $\hat{E}^*$  (Eqn. (21)). The former represents layers bonded to the rigid plates directly, and the latter represents layers bonded to the rigid plates via compliant interphases. We define the sensitivity to the in-

$$S:=1-\frac{\widehat{E}^*}{\widehat{F}}.$$

Accordingly, very stiff, practically undetectable, interphases, are characterized by  $S \ll 1$ . Conversely, soft, detectable, interphases are characterized by S slightly less than one. Sensitivity contour plots for 50  $\mu m$ 

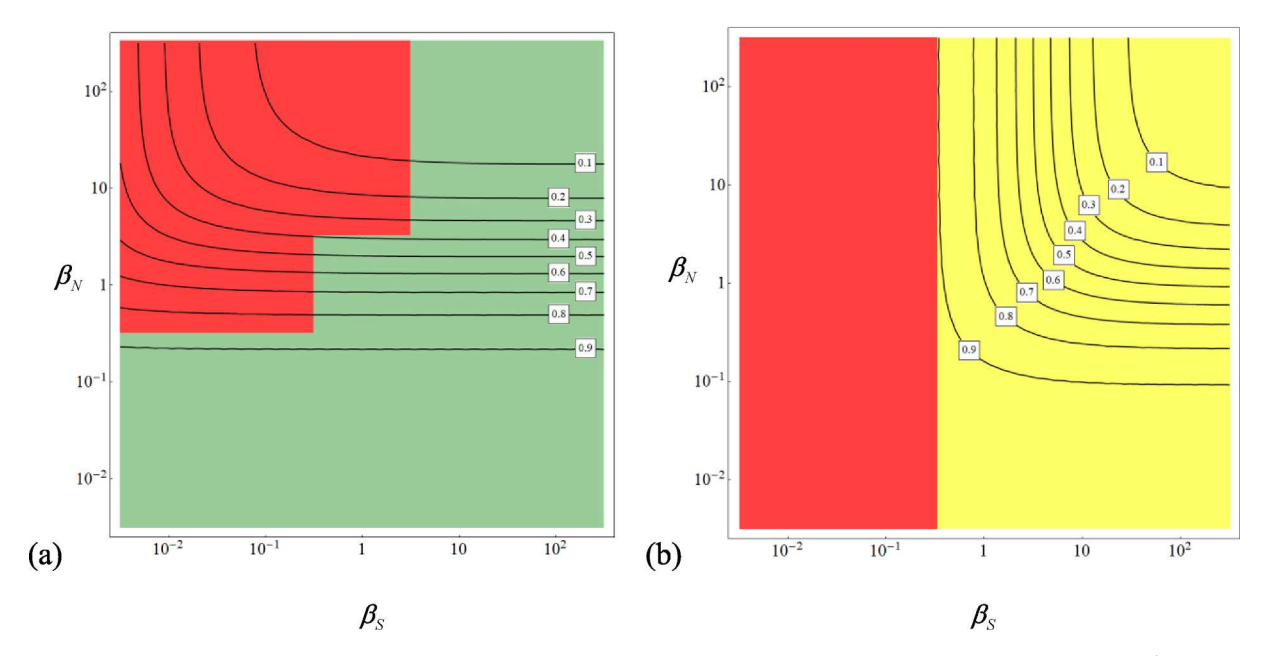


**Fig. 8.** Sensitivity *S* contour plots for  $50\mu m$  thick epoxy (a) and rubber (b) layers. The colors are assigned as follows: (*i*) red if the error for both  $\widehat{E}^*$  and  $\overline{E}^*$  exceeds 1%, (*ii*) yellow if the error for  $\overline{E}^*$  but not  $\widehat{E}^*$  exceeds 1%, and (*iii*) green if the error for both  $\widehat{E}^*$  and  $\overline{E}^*$  is less than 1%. (For interpretation of the references to color in this figure legend, the reader is referred to the Web version of this article.)

thick epoxy and rubber layers are shown in Fig. 8. There we plot S as a function of the normalized stiffnesses  $\beta_N$  and  $\beta_S$ . In addition, we include results from Tables 2 and 3 to define the parametric subdomains in which  $\widehat{E}^*$  is a valid approximation. This allows us to identify properly constrained layers suitable for measuring  $k_N$  and  $k_S$ .

It is clear that for both epoxy and rubber there is essentially no conflict between the accuracy of the asymptotic solution and sensitivity S. Note that in Fig. 8a the contour plots become flat for sufficiently large  $\beta_S$ . Those represent the regime where  $\widehat{E}^*$  and  $\overline{E}^*$  become interchangeable, and of course the flatness is consistent with the fact that per (22)  $\overline{E}^*$  is independent of  $\beta_S$ . In contrast, the flatness does not persist in Fig. 8b, and this is not surprising, as  $\overline{E}^*$  is not a good approximation for nearly incompressible rubber layers.

Let us mention that the measurements of  $k_N$  and  $k_S$  reported by Yang et al. (2021), who used 50  $\mu$ m thick epoxy layers result in  $\beta_N=0.056$  and  $\beta_S=0.7$ . For this point,  $\overline{E}^*$  is an accurate approximation and the interphases are easily detectable as S>0.9. On the other hand, given that rubber interphases tend to be much stiffer than the bulk rubber, we can see that they will be more difficult or even impossible to detect.

An interesting feature of interphases in nearly incompressible layers is their impact on the strain and stress fields. The asymptotic solution developed in Section 3.2 allows us to consider several quantities of interest and various ways of presenting results. The upshot of those studies is that interphases reduce non-uniformity of the strain and stress fields, and therefore inhibit the ability of thin rubber layers to realize stress concentrations leading to cavitation.

The most important stress component associated with cavitation is the average normal stress defined as

$$\sigma:=\frac{1}{3}\mathrm{tr}\sigma_{ij}.$$

For incompressible layers perfectly bonded to rigid plates, this stress is very large indeed,

$$\sigma^{(0)} \simeq \frac{U\mu}{4a\xi^3} = \left(3\mu \frac{U}{h}\right) \times \left(\frac{1}{12\xi^2}\right). \tag{32}$$

This expression can be obtained in the limit  $\chi \to 0$ ,  $\beta_N \to \infty$ ,  $\beta_S \to \infty$ . The

second part of the expression implies that perfect bonding amplifies  $\sigma$  by a factor  $\xi^{-2}/12$  in comparison to uniaxial tension realized by perfectly lubricated plates. We regard (32) as a benchmark stress level induced upon imposing all three constraints characterized by the limit  $\chi \to 0$ ,  $\beta_N \to \infty$ ,  $\beta_S \to \infty$ . In what follows, we relax one constraint at a time and quantify its effect on a rubber layer with  $\xi = 0.01$ . All results are obtained from the solution presented in Section 3.2.

First, we set  $\chi=0.024$ , which corresponds to  $\nu=0.499905$ , and retain the limit  $\beta_N\!\to\!\infty,\ \beta_S\!\to\!\infty$ . The corresponding value of  $\sigma$  is

$$\sigma^{(1)} \approx 0.47 \sigma^{(0)}$$
.

Thus if rubber is assumed to be incompressible, the stress is overestimated roughly by a factor of two. Next, we retain  $\chi=0.024$  and the perfect shear constraint  $\beta_S{\to}\infty$ , and evaluate the corresponding  $\sigma$  normalized by  $\sigma^{(1)}$  as a function of  $\beta_N$ . The range of  $\beta_N$  chosen in Fig. 9 demonstrates that even  $\beta_N=10^3$  results in more than a 20% reduction in  $\sigma$  in comparison to  $\sigma^{(1)}$ . Finally, let us retain  $\chi=0.024$ , set  $\beta_N{\to}\infty$ , and evaluate the corresponding  $\sigma$  normalized by  $\sigma^{(1)}$  as a function of  $\beta_S$ . The range of  $\beta_S$  chosen in Fig. 10 demonstrates that even for  $\beta_S=100$ , the reduction in  $\sigma$  in comparison to  $\sigma^{(1)}$  is only about 1%. Thus,

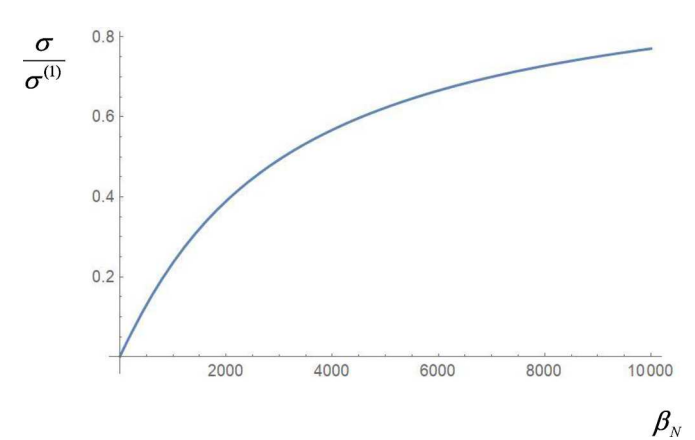


**Fig. 9.** The normalized stress  $\sigma/\sigma^{(1)}$  as a function of  $\beta_N$  for a rubber layer with  $\xi=0.01$  and  $\beta_S\!\to\!\infty$ .

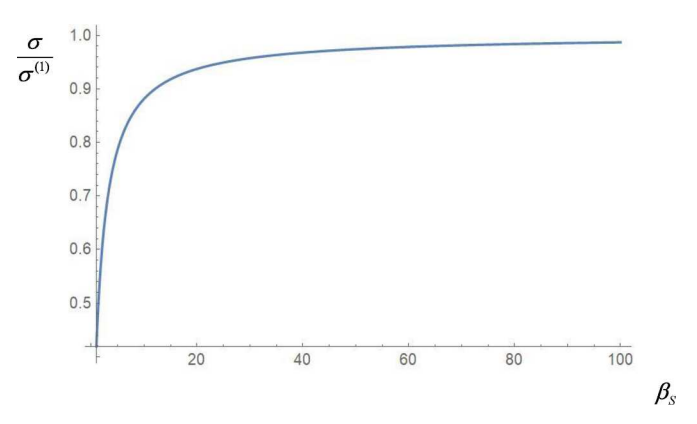


**Fig. 10.** The normalized stress  $\sigma/\sigma^{(1)}$  as a function of  $\beta_S$  for a rubber layer with  $\xi = 0.01$  and  $\beta_N \to \infty$ .

mechanical characterization of thin rubber layers must account for their compressibility and the normal stiffness of their interphases; the shear stiffness of the interphases must be sufficiently large to provide proper constraints, but insignificant otherwise.

In summary, we proposed a new experimental setup for probing interphases. It involves a thin polymeric layer bonded to two very stiff plates. The experimental setup was analyzed under the assumption that the layer and interphase are linear elastic and the plates are rigid. We demonstrated that for compressible layers, which represent most polymers, the governing equations are particularly simple, and can be extended to analysis of multilayers with or without interphases. Further, we identified the parametric range in which our approach is applicable and interphases are detectable via load-displacement measurements. Once experimental data become available, it will significantly impact existing modeling approaches to interphases (Gurtin and Murdoch, 1975, 1978; Ru, 2010) and composites (Lipton and Vernescu, 1996; Klarbring and Movchan, 1998; Hashin, 2002; Benveniste, 2006).

#### Author agreement statement

We the undersigned declare that this manuscript is original, has not been published before and is not currently being considered for publication elsewhere. We confirm that the manuscript has been read and approved by all named authors and that there are no other persons who satisfied the criteria for authorship but are not listed. We further confirm that the order of authors listed in the manuscript has been approved by all of us. We understand that the Corresponding Author is the sole contact for the Editorial process. He is responsible for communicating with the other authors about progress, submissions of revisions and final approval of proofs.

#### Declaration of competing interest

The authors declare that they have no known competing financial interests or personal relationships that could have appeared to influence the work reported in this paper.

#### Acknowledgements

GJR and KRR acknowledge financial support through the projects MCTool<sup>21</sup> (6305-1452/1490) co-financed by the European Regional Development Fund through the Operational Program for Competitiveness and Internationalization COMPETE 2020, the North Portugal Regional Operational Program NORTE 2020, and by the Portuguese Foundation for Science and Technology FCT under the UT Austin Portugal Program. KML acknowledges financial support through the National Science Foundation Grant CMMI 2110526.

#### References

- Anderson, M., Mott, P., Roland, C., 2004. The compression of bonded rubber disks. Rubber Chem. Technol. 77, 293–302.
- Barenblatt, G.I., 1959. The formation of equilibrium cracks during brittle fracture.

  General ideas and hypotheses. Axially-symmetric cracks. J. Appl. Math. Mech. 23,
- Benveniste, Y., 2006. A general interface model for a three-dimensional curved thin anisotropic interphase between two anisotropic media. J. Mech. Phys. Solid. 54, 708–734
- Bouchet, J., Roche, A.-A., 2002. The formation of epoxy/metal interphases: mechanisms and their role in practical adhesion, J. Adhes, 78, 799–830.
- Brune, P.F., Blackman, G.S., Diehl, T., Meth, J.S., Brill, D., Tao, Y., Thornton, J., 2016.
  Direct measurement of rubber interphase stiffness. Macromolecules 49, 4909–4922.
- Chalhoub, M.S., Kelly, J.M., 1990. Effect of bulk compressibility on the stiffness of cylindrical base isolation bearings. Int. J. Solid Struct. 26, 743–760.
- Dey, M., Deitzel, J., Gillespie Jr., J., Schweiger, S., 2014. Influence of sizing formulations on glass/epoxy interphase properties. Compos. Appl. Sci. Manuf. 63, 59–67.
- Dillard, D.A., Mukherjee, B., Karnal, P., Batra, R.C., Frechette, J., 2018. A review of Winkler's foundation and its profound influence on adhesion and soft matter applications. Soft Matter 14, 3669–3683.
- Drzal, L.T., 1986. The interphase in epoxy composites. Adv. Polym. Sci. 75, 71-32.
- Drzal, L.T., Rich, M.J., Floyd, P.F., 1982. Adhesion of graphite fibers to epoxy matrices I, the role of fiber surface treatment. J. Adhes. 16, 1–30.
- Drzal, L.T., Rich, M.J., Floyd, P.F., 1983. Adhesion of graphite fibers to epoxy matrices II: the effect of fiber finish. J. Adhes. 16, 133–152.
- Dugdale, D.S., 1960. Yielding of steel sheets containing slits. J. Mech. Phys. Solid. 8, 100–104.
- Gent, A., 1994. Compression of rubber blocks. Rubber Chem. Technol. 67, 549–558.
   Gent, A.N., Lindley, P.B., 1959. The compression of bonded rubber blocks. Proc. Inst. Mech. Eng. 173, 111–122.
- Gorbushin, N., Eremeyev, V.A., Mishuris, G., 2020. On stress singularity near the tip of a crack with surface stresses. Int. J. Eng. Sci. 146, 103183.
- Gowrishankar, S., Mei, H., Liechti, K.M., Huang, R., 2012. Comparison of direct and iterative methods for determination of silicon/epoxy interface traction-separation relations. Int. J. Fract. 177, 109–128.
- Gurtin, M.E., Murdoch, A.I., 1975. A continuum theory of elastic material surfaces. Arch. Ration. Mech. Anal. 57, 291–323.
- Gurtin, M.E., Murdoch, A.I., 1978. Surface stress in solids. Int. J. Solid Struct. 14, 431–440.
- Hashin, Z., 2002. Thin interphase/imperfect interface in elasticity with application to coated fiber composites. J. Mech. Phys. Solid. 50, 2509–2537.
- Horton, J., Tupholme, G.E., Gover, M.J., 2002. Axial loading of bonded rubber blocks. J. Appl. Mech. 69, 836–843.
- Kim, C., Schiavone, P., Ru, C.-Q., 2011a. Effect of surface elasticity on an interface crack in plane deformations. Proc. Math. Phys. Eng. Sci. 467, 3530–3549.
- Kim, C.I., Schiavone, P., Ru, C.-Q., 2011b. Analysis of plane-strain crack problems (mode-I & mode-II) in the presence of surface elasticity. J. Elasticity 104, 397–420. Klarbring, A., Movchan, A., 1998. Asymptotic modelling of adhesive joints. Mech. Mater.
- 28, 137–145.

  Kozlov, V., Maz'Ya, V.V., Maz'ia, V.G., Maz'ia, V., Maz'ya, V., Movchan, A.B., 1999.

  Asymptotic Analysis of Fields in Multi-Structures. Oxford University Press on
- Liechti, K.M., Shirani, A., Dillingham, R.G., Boerio, F.J., Weaver, S.M., 2000. Cohesive zone models of polyimide/aluminum interphases. J. Adhes. 73, 259–297.
- Lindley, P.B., 1979. Compression moduli for blocks of soft elastic material bonded to rigid end plates. J. Strain Anal. Eng. Des. 14, 11–16.
- Lindsey, G.H., Schapery, R.A., Williams, M.L., Zak, A.R., 1963. The Triaxial Tension Failure of Viscoelastic Materials. Aerospace Research Laboratories.
- Lipton, R., Vernescu, B., 1996. Composites with imperfect interface. In: Proceedings of the Royal Society of London. Series A: Mathematical, Physical and Engineering Sciences, vol. 452, pp. 329–358.
- Maz'ya, V., Movchan, A., Nieves, M., 2013. Green's Kernels and Meso-Scale Approximations in Perforated Domains. Springer.
- Mello, A.V., Liechti, K.M., 2006. The effect of self-assembled monolayers on interfacial fracture. J. Appl. Mech. 73, 860–870.
- Movchan, A.B., Movchan, N.V., 1995. Mathematical Modelling of Solids with Nonregular Boundaries. CRC Press.
- Movchan, A.B., Movchan, N.V., Jones, I.S., Colquitt, D.J., 2017. Mathematical Modelling of Waves in Multi-Scale Structured Media. CRC Press.
- Movchan, A.B., Movchan, N.V., Poulton, C.G., 2002. Asymptotic Models of Fields in Dilute and Densely Packed Composites. World Scientific.
- Movchan, A.B., Rebrov, K.R., Rodin, G.J., 2021. Axisymmetric deformation of compressible, nearly incompressible, and incompressible thin layers between two rigid surfaces. Int. J. Solid Struct. 214, 61–73.
- Needleman, A., 1990. An analysis of tensile decohesion along an interface. J. Mech. Phys. Solid. 38, 289–324.
- Ockendon, J.R., Howison, S., Lacey, A., Movchan, A., 2003. Applied Partial Differential Equations. Oxford University Press on Demand.
- Park, K., Paulino, G.H., 2011. Cohesive zone models: a critical review of tractionseparation relationships across fracture surfaces. Appl. Mech. Rev. 64.
- Qi, Y., Jiang, D., Ju, S., Zhang, J., Cui, X., 2019. Determining the interphase thickness and properties in carbon fiber reinforced fast and conventional curing epoxy matrix composites using peak force atomic force microscopy. Compos. Sci. Technol. 184, 107877.

### ARTICLE IN PRESS

#### K.M. Liechti et al.

European Journal of Mechanics / A Solids xxx (xxxx) xxx

- Qiao, S., Lu, N., 2015. Analytical solutions for bonded elastically compressible layers. Int. J. Solid Struct. 58, 353–365.
- Roche, A., Bouchet, J., Bentadjine, S., 2002. Formation of epoxy-diamine/metal interphases. Int. J. Adhesion Adhes. 22, 431–441.
- Ru, C., 2010. Simple geometrical explanation of Gurtin-Murdoch model of surface elasticity with clarification of its related versions. Sci. China Phys. Mech. Astron. 53, 536–544.
- Schapery, R., 2018. Elastomeric bearing sizing analysis Part 2: flat and cylindrical bearings. Int. J. Solid Struct. 152, 140–150.
- Sharpe, L.H., 1972. The interphase in adhesion. J. Adhes. 4, 51-64.
- Sorensen, B.F., Jacobsen, T.K., 2003. Determination of cohesive laws by the J integral approach. Eng. Fract. Mech. 70, 1841–1858.
- Sorensen, B.F., Kirkegaard, P., 2006. Determination of mixed mode cohesive laws. Eng. Fract. Mech. 73, 2642–2661.
- Tian, C., Chu, G., Feng, Y., Lu, Y., Miao, C., Ning, N., Zhang, L., Tian, M., 2019. Quantitatively identify and understand the interphase of SiO2/rubber

- nano<br/>composites by using nanomechanical mapping technique of AFM. Compos. Sci. Technol. 170,<br/>  $1\!-\!6.$
- Tsai, H.-C., Lee, C.-C., 1998. Compressive stiffness of elastic layers bonded between rigid plates. Int. J. Solid Struct. 35, 3053–3069.
- Ungsuwarungsri, T., Knauss, W.G., 1987. The role of damage-softened material behavior in the fracture of composites and adhesives. Int. J. Fract. 35, 221–241.
- Vanlandingham, M.R., Eduljee, R.F., Gillespie Jr., J.W., 1999. Relationships between stoichiometry, microstructure, and properties for amine-cured epoxies. J. Appl. Polym. Sci. 71, 699–712.
- Wu, C., Huang, R., Liechti, K.M., 2019. Simultaneous extraction of tensile and shear interactions at interfaces. J. Mech. Phys. Solid. 125, 225–254.
- Yang, T., Gandhi, V., Huang, R., Liechti, K.M., 2021. Rate dependent fracture along a silicon/epoxy interface under mixed-mode loading conditions. Int. J. Solid Struct. 111129.
- Zhang, M., Li, Y., Kolluru, P.V., Brinson, L.C., 2018. Determination of mechanical properties of polymer interphase using combined atomic force microscope (AFM) experiments and finite element simulations. Macromolecules 51, 8229–8240.